Pergamon

Journal of Structural Geology, Vol. 19, Nos 3–4, pp. 303 to 319, 1997

PII: S0191-8141(96)00090-9
0191-8141/97 $17.00 + 0.00

Origin of a thrust-related fold: geometric vs kinematic tests

KAREN L. THORBJORNSEN and WILLIAM M. DUNNE*

Department of Geological Sciences, University of Tennessee, Knoxville, TN 37996-1410, U.S.A.

(*Received* 2 *February* 1996; *accepted in revised form* 8 *October* 1996)

Abstract—Geometric tests to determine the origin of fault-related folds are common, but as is typical in structural geology, more than one fold origin may yield the final natural geometry. Thus, the results of geometric tests are usually non-unique. In contrast, kinematic tests of origin, which employ both geometry and data about deformation, commonly yield more constrained, if not unique, results. Unfortunately, the necessary data collection requires much more work than for a geometric test. In this study, the thrust-related Barclay anticline is analyzed both geometrically and kinematically to determine which test is more effective. Geometric tests, using angular relationships, indicate three possible origins: fault-bend, fault-arrest, and break-thrust. For the kinematic test, predicted deformations for interlayer and flexural slip, flexural flow, simple shear, and bending strains are compared to micro- and mesostructural distributions, solution strain, and finite strain from the anticline. Strain measurements indicate that microscale deformation is uniformly distributed through the structure and is lithification-dominated. The microscale deformation does not match kinematic predictions, and did not accommodate fold formation. Fold growth was achieved primarily through layer-parallel slip restricted mostly to the forelimb and absent in the hinge, which eliminates fault-bend and fault-arrest origins that require material transport from forelimb to backlimb. The Barclay anticline is therefore interpreted to be a break-thrust structure. Interestingly, a suite of contraction faults in the forelimb and hinge indicates material transport from forelimb to backlimb. Such transport has been discounted for break-thrust folds. The most important result of this study is that a kinematic test was a necessary step for distinguishing fold origin. Geometric testing alone was insufficient. Given that the Barclay anticline has geometric characteristics typical of many thrust-related folds, kinematic testing appears necessary to determine their structural origin.

INTRODUCTION

The origin of fault-related folds may be described by using one of a series of kinematic models that have characteristic geometries and explicit assumptions about the behavior of deformed rocks (Table 1). Geometric tests are commonly used to determine the kinematic origin of most fault-related folds (Willis, 1893; Suppe, 1983; Williams and Chapman, 1983; Jamison, 1987; Suppe and Medwedeff, 1990; Morley, 1994) (Table 1). In a geometric test, attributes of a fold such as interlimb angle and limb dip are compared to predicted values from a particular fold model. The inherent weakness in this approach is that more than one model may yield the same geometry, since "final geometry does not necessitate a particular deformation history" (Passchier *et al.*, 1992). Another approach for determining the kinematic origin of a fault-related fold is the kinematic test. This test compares predicted deformation sequences from a model to measured incremental and finite strain indicators, kinematic indicators on slip surfaces, and cross-cutting relationships. Although kinematic tests have revealed unique origins for fault-related folds (Armstrong and Bartley, 1993; Fisher and Anastasio, 1994), this type of test is seldom used (Table 1).

By comparing a suite of models to a field example, this paper examines the effectiveness of geometric tests as discriminators for the origin of fault-related folds. The geometry of the field example is shown to be consistent with four possible origins, illustrating the limitations of a purely geometric analysis of fold evolution. Subsequently, a kinematic analysis of the fold is applied to reduce the number of possible solutions to one.

Models for fault-related folds

A convenient way to classify fault-related folds is in terms of their timing with respect to fault propagation (Suppe and Medwedeff, 1990) (Table 1). The most popular model for folds that precede fault propagation is break-thrust folding (Willis, 1893), where fold shape need not depend on fault geometry (Fig. 1a). Another less commonly applied model is the stretch fold that was first identified in the Alps (Heim, 1921), where a recumbent nappe forms and intense shear in the overturned limb of the anticline leads to faulting in that limb. Thus, the fault is necessitated by localized intense deformation during folding.

Fault-propagation folding (Suppe and Medwedeff, 1990) is a popular kinematic explanation for folds that form during propagation of imbricate faults (Fig. 1b). This morphology was originally described as a subset of tip-line folds (Williams and Chapman, 1983), but that terminology is not generally used. A key feature of fault-propagation folding is that fault shape constrains fold shape. Detachment folds may also develop during fault propagation, but the fault is a bed-parallel flat rather than an imbricate (Jamison, 1987; Dahlstrom, 1990). Detachment folds are either folds that amplify as thrust

*To whom correspondence should be addressed.

Table 1. Kinematic models for the origin of fault-related folds

	Kinematically/mechanically tested	Assumed or geometrically tested*
1. Break-thrust fold	Mitchell and Woodward (1988); Fischer *et al.* (1992)	Willis (1893); Butler (1992); Woodward (1992); Morley (1994)
2. Stretch thrust		Heim (1921)
3. Fault-propagation fold (some tip-line folds)	Couzens and Dunne (1994); Fisher and Anastasio (1994); Tavarnelli (1994)	Williams and Chapman (1983); Chapman and Williams (1984); Yeats *et al.* (1988); Suppe and Medwedeff (1990); Mitra (1990); Erslev (1991); Jamison (1992); Mountjoy (1992); Alonso and Teixell (1992); Suppe *et al.* (1992); Al Saffar (1993); McNaught and Mitra (1993); Schmidt *et al.* (1993); Dominic and McConnell (1994); McConnell (1994); Narr and Suppe (1994); Moustafa and Khalil (1995)
4. Detachment folds		Laubscher (1976); Wiltschko and Chapple (1977); Jamison (1987); Mitra and Namson (1989); Dahlstrom (1990); Jamison (1992); Groshong and Epard (1994); Hennings (1994); Hardy and Poblet (1994); Homza and Wallace (1995)
5. Fault-bend fold	Wiltschko *et al.* (1985); Kilsdonk and Wiltschko (1988)	Rich (1934); Suppe (1983); Cooper *et al.* (1983); Cello *et al.* (1989); McDougall and Hussain (1991); Schelling and Arita (1991); Jamison (1992); Medwedeff (1992); Ramsay (1992); Zoetemeijer *et al.* (1992); Onasch and Dunne (1993); Jadoon *et al.* (1994); Hippolyte *et al.* (1994); Srivastava and Mitra (1994); Parfenov *et al.* (1995)
6. Fault-arrest fold (some tip-line folds)	Armstrong and Bartley (1993); Hedlund *et al.* (1994) (possibly a fault-bend fold)	Williams and Chapman (1983); Chapman and Williams (1984); Wickham (1995)

* This column of citations is only meant to be representative and not exhaustive of the many studies using this approach. Younger citations are deliberately favored.

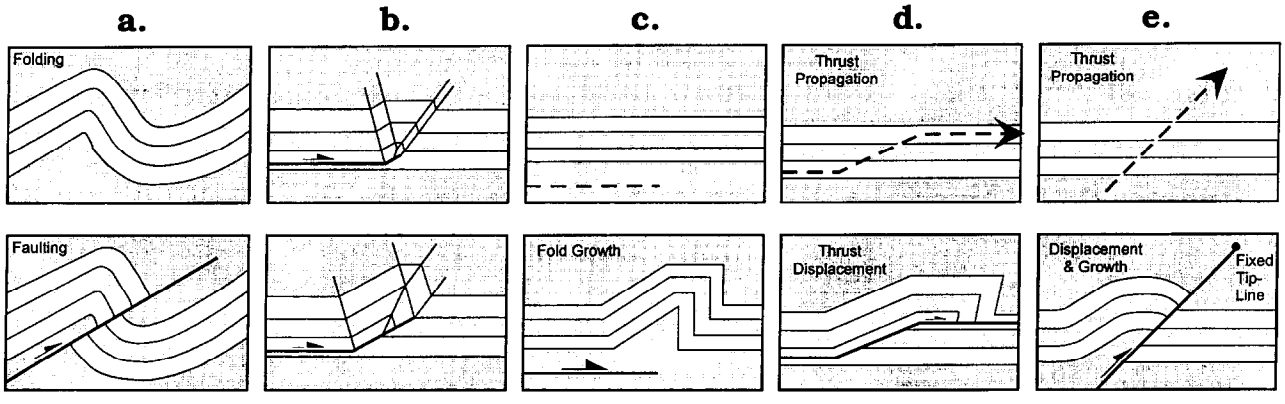

Fig. 1. Simple time sequences for different models of thrust-related folding. (a) Break-thrust fold. (b) Fault-propagation fold. (c) Detachment fold. (d) Fault-bend fold. (e) Fault-arrest fold.

displacement accrues near a thrust tip (Fig. 1c) or buckle folds that develop between bounding décollements. Geometry of detachment folds depends on detachment depth and shortening (Groshong and Epard, 1994; Homza and Wallace, 1995).

Perhaps the most commonly illustrated fault-related fold is the fault-bend fold (Rich, 1934) (Fig. 1d). This structure postdates fault propagation and its geometry is a function and result of the change in fault trajectory (Suppe, 1983). Another type of fault-related folding that postdates fault-propagation has been recently recognized (Armstrong and Bartley, 1993; Wickham, 1995). The defining characteristic of this model is that the tip of an imbricate fault remains stationary while displacement continues (Fig. 1e). A deformation discontinuity is avoided around the fault tip by a fold amplifying in the hangingwall to absorb the accumulating displacement. Some 'tip-line folds' (Williams and Chapman, 1983) and 'displacement-gradient folds' (Wickham, 1995) have this behavior. This behavior was also proposed to explain the development of a fold in the hangingwall of the Golden Gate thrust, Nevada (Armstrong and Bartley, 1993). We propose that these structures be called 'fault-arrest folds' to denote that they develop when the fault tip is stationary but while the thrust is still displacing. As was indicated by Williams and Chapman (1983) with tip-line folds, a continuum of behavior exists between propagating faults with no displacements and displacing faults with no propagation, but this proposed term defines a useful end-member behavior. These different classes of folds (Table 1; Fig. 1) will be used as end-member geometries and kinematic behaviors to be tested against

the measured geometries and kinematic behaviors of our field example.

THE FIELD EXAMPLE

Geological setting

The study area is in southeastern West Virginia in the Plateau of the central Appalachians (Fig. 2). The thrust-related fold under scrutiny, the Barclay anticline, is located in the Browns Mountain anticlinorium (Kulander, 1968; Cecil, 1972; Kulander *et al.*, 1986).

The anticline deformed the Lower Silurian Tuscarora Sandstone, a planar- to cross-bedded, locally burrowed, well-sorted quartz arenite (Reger and Price, 1926; Reger, 1931; Cecil, 1972; Kulander *et al.*, 1986; Bambach, 1987; Dorsch *et al.*, 1994). The 47-m thickness of the Tuscarora Sandstone is divisible into two distinct units. The 25-m lower Tuscarora Sandstone consists of medium- to coarse-grained, thin- to medium-bedded sandstone with some thin siltstone interbeds and a basal pebble conglomerate. The upper unit consists of medium- to coarse-grained, thin- to thick-bedded sandstone. Within this upper unit are two intervals of mudstone and siltstone, 3 m and 6 m in thickness, respectively. These two intervals are informally known as 'racetracks' and they separate the Sandstone into three mechanical struts. The Tuscarora Sandstone was buried about 5.5 km by a Silurian to possibly Permian sequence (Colton, 1970; Chen, 1981), and reached peak temperatures of 150–200°C, as determined from conodont color-alteration indices in overlying Silurian limestones (Harris, 1979).

The Ordovician Juniata Formation underlies the Tuscarora Sandstone and consists of terrigeneous red sandstone and shale. The overlying Middle Silurian Rose Hill Formation consists of a lower unit of hematite-cemented quartz sandstone and an upper unit of olive-green to brown shales and thin siltstone beds.

Structural geometry of the Barclay anticline

The changes in geometry of the Barclay anticline are illustrated in two cross-sections across the structure (Figs 2 & 3). The constraints for cross-section construction were: (1) surface geology, including abundant exposures of Tuscarora Sandstone with bedding orientation data, some stratigraphic contacts, and clearly exposed fold geometry; (2) stratigraphic thickness of about 47 m for the Tuscarora Sandstone as obtained from an exposed section with a uniform dip of 55°SE within 1 km of field area; (3) the constant thickness of the sandstone throughout the fold; (4) the topographic rise to the southwest of the anticlinal crest in the hangingwall, as compared to the

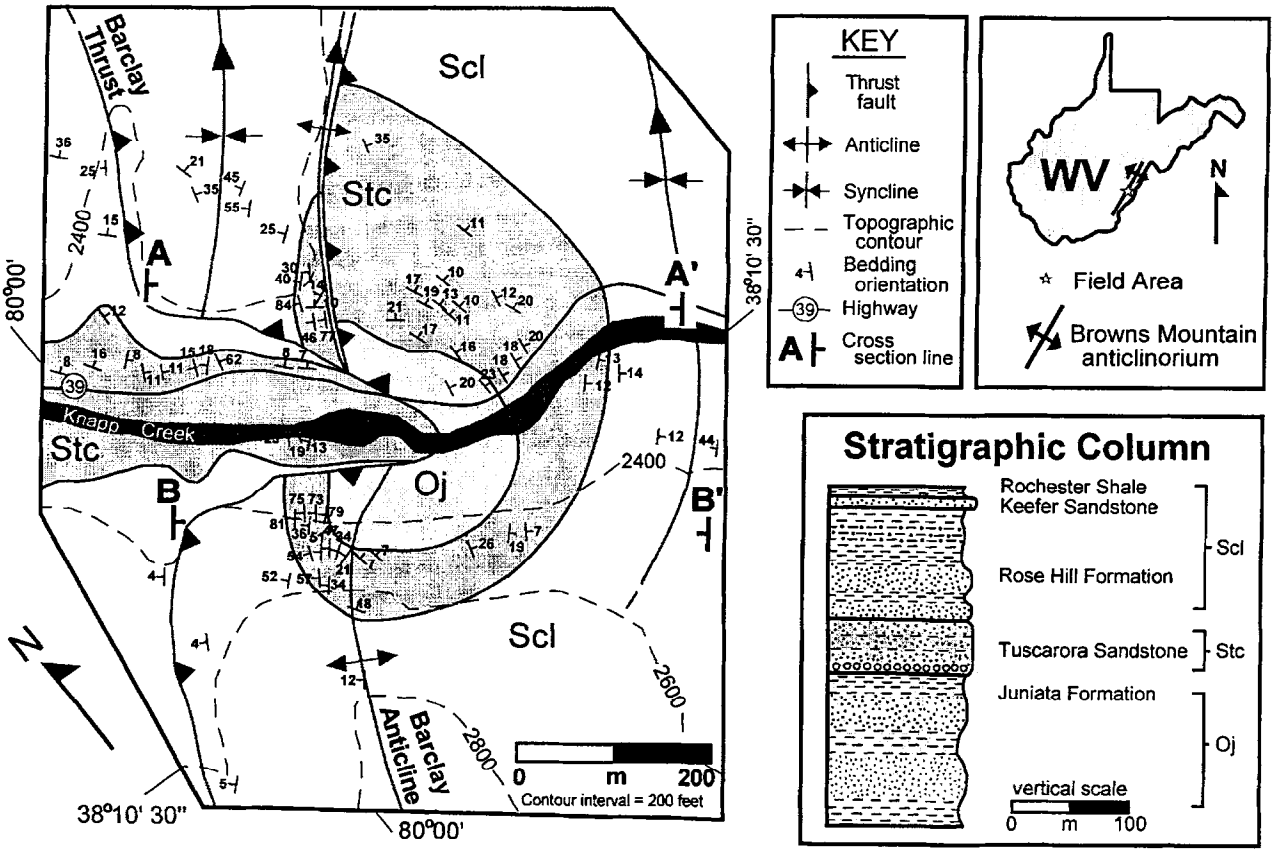

Fig. 2. Geological map and stratigraphic column for study area, showing locations of section lines in Fig. 3.

constant elevation of the top of the Tuscarora Sandstone in the footwall; and (5) an additional stratigraphic juxtaposition of hangingwall rocks in the northern profile, which indicates the presence of an additional imbricate thrust there. The assumptions for section construction were: (1) a parallel fold style, which is consistent with field observations; (2) the Barclay thrust predates smaller folds in the footwall, and hence is folded by them; (3) the stratigraphic interval between the Tuscarora Sandstone of the footwall and hangingwall is occupied almost entirely by Juniata Formation of the hangingwall, defining depth to floor thrust; (4) the dip of bedding in the hangingwall is representative of the dip of the thrust, except beneath the hangingwall ramp; and (5) the bedding at the unexposed footwall ramp is initially inferred to be flat, because the closest exposed footwall rocks are flat-lying at a distance of 130 m from the nearest exposed hangingwall rocks (Fig. 2). We emphasize that the footwall ramp is unexposed, so the footwall cutoff geometry and ramp dip are not fully constrained by the existing data.

As seen in both cross-sections, the anticline has a subvertical forelimb, a rounded hinge, and a backlimb that gently steepens to about a 20°SE dip above the footwall ramp. The thrust and anticline geometry change over the 250 m between the two profiles. In the plunge-out direction to the northeast, displacement decreases along the fault by 35 m, the footwall ramp shallows slightly, depth to detachment in the Juniata Formation and fold amplitude decrease by about 25 m, and an imbricate thrust appears adjacent to the hinge. The imbricate thrust in the northern profile is interpreted to have formed during or prior to folding because the fault does not offset footwall rocks.

GEOMETRIC TEST

The Barclay anticline has many of the typical features of a thrust-related fold: steep forelimb, a gently dipping backlimb that is locally subhorizontal, subhorizontal beds in the footwall, and a footwall ramp angle $<30°$. Formation of the Barclay anticline has included a component of fault-bend folding (Fig. 3), because rocks were transported over a ramp. Yet, this structure need not have initiated as a fault-bend fold, so, geometric analysis is required to determine origin. The structure is not a stretch thrust because it lacks a recumbent isoclinal geometry (Heim, 1921). The structure is not a detachment fold because it does not overlie a thick décollement horizon (Laubscher, 1976; Wiltschko and Chapple, 1977; Homza and Wallace, 1995). Thus, the four surviving models of fault-propagation, fault-bend, fault-arrest, and break-thrust folding will be considered during geometric testing for fold origin.

Several authors have presented graphs for determining geometrically the origin of thrust-related folds (Suppe, 1983; Jamison, 1987; Mitra, 1990; Suppe and Medwedeff, 1990; Homza and Wallace, 1995). The present authors believe that the most coherent graph set is that proposed

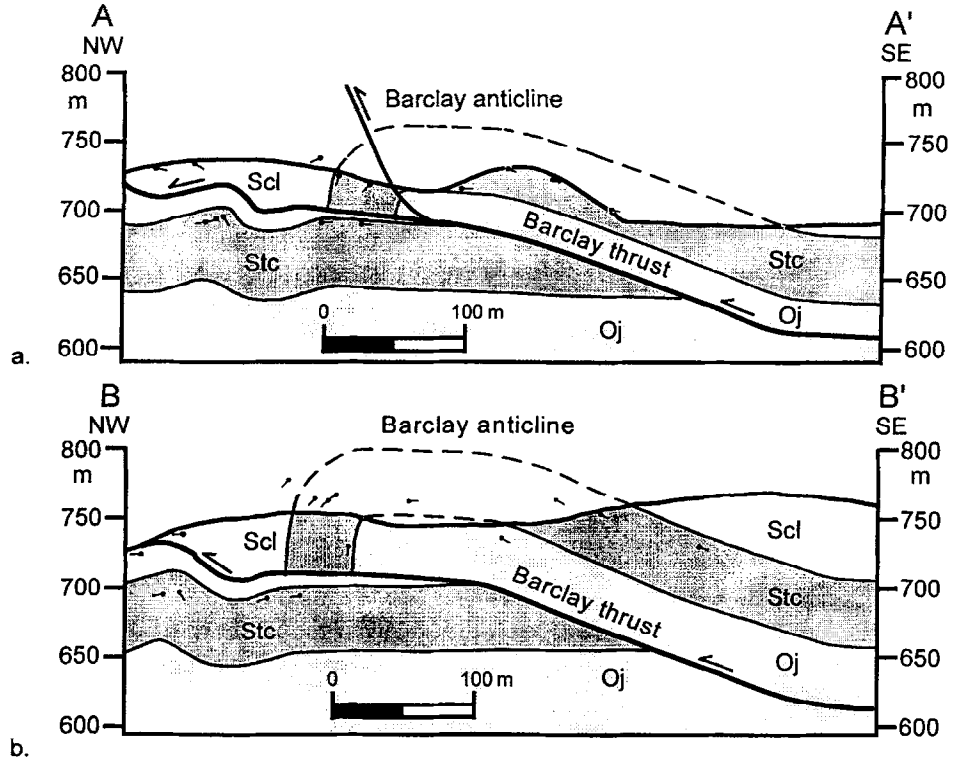

Fig. 3. Section lines across Barclay anticline and thrust. (a) Northern profile AA'. (b) Southern profile BB' (see Fig. 2 for stratigraphic ornaments and section locations).

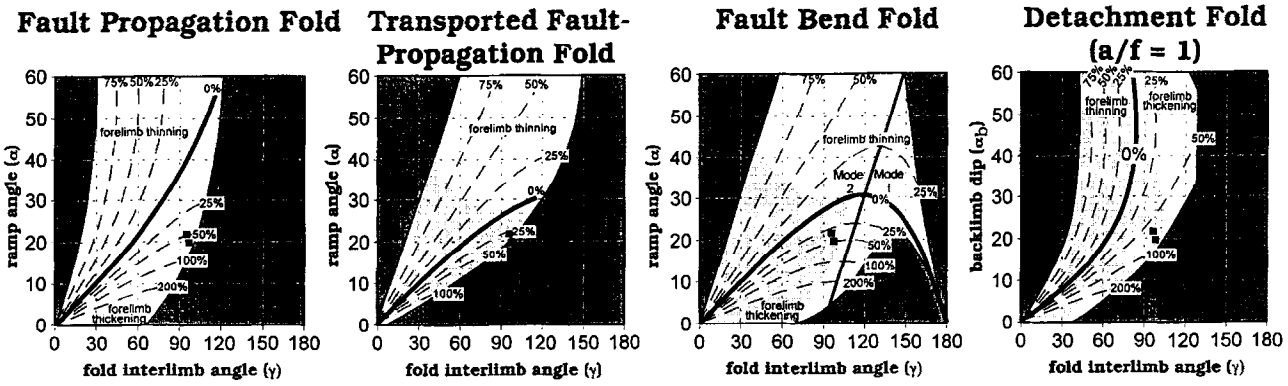

Fig. 4. Graphs of angular characteristics for geometric models of thrust-related folds. The stippled fields show where a 25% error in measuring unit thickness causes an overlap in prediction between that model and fault-propagation folding (filled squares — values for Barclay anticline from profiles AA′ and BB′. Thick curve — ideal geometry with no thickness variation. Contour values are percent change in bed thickness) (modified from Jamison, 1987).

by Jamison (1987) because it considers several different models. Plotting geometric data from the Barclay anticline on these graphs shows that the Tuscarora Sandstone should have thickened by 25–70% in the anticlinal forelimb if the anticline formed by fault-propagation, fault-bend, or transported fault-propagation folding (Fig. 4). The sandstone preserves original thickness in the forelimb, so one might conclude that this fold is not one of these types of structures. An alternative conclusion is that one or more of the models might apply if they deviate from ideal geometry (thick curves, Fig. 4) by an artifact other than the forelimb thickness variation as used by Jamison (1987). Possible deviations that preserve layer thickness are subsidiary thrusts and layer-parallel slip or shear, which would alter the distribution of limb length through the fold without changing the total limb length.

We chose to consider these deviations by using the geometry of the southern profile (Fig. 3b) as the constraint. This choice eliminated subsidiary thrusts because they are absent. Layer-parallel slip or shear changes limb length in the forelimb when rock migrates through the fold hinge from forelimb to backlimb (Fig. 5). This change in forelimb length is the deviation from ideal behavior that allows fault-propagation, fault-bend, fault-arrest and break-thrust models to remain possibly applicable to the Barclay anticline.

Profiles were constructed as a geometric test of each model that preserved layer thickness, allowed layer-parallel displacements and matched existing geometry (Figs 3 & 6). One model could not geometrically satisfy these restrictions: fault-propagation folding (Fig. 6a). While many geometric variants of fault-propagation folding exist (Mitra, 1990; Suppe and Medwedeff, 1990; McConnell, 1994), the only applicable one must exhibit constant layer-thickness. This variant yields a geometry that has too tight an interlimb angle when compared to field observations and requires an overturned limb, which is absent. Additionally, as the fold transported over the upper bend of a footwall ramp, a second fold hinge and an axial surface should appear above the roof flat (Fig. 6a). The natural fold profile lacks such features (Fig. 6a vs. Fig. 3b). Fault-bend, fault-arrest, and break-thrust folding yield admissible geometries, so these models may explain fold origin if forelimb length may be varied during folding. Still, this geometric test does not identify a single origin for the Barclay anticline, and an additional test is necessary to determine a unique origin.

KINEMATIC TEST

The three remaining models for thrust-related folding may be used to predict deformation distributions within the Barclay anticline (Suppe, 1983; Mitra, 1990; Suppe

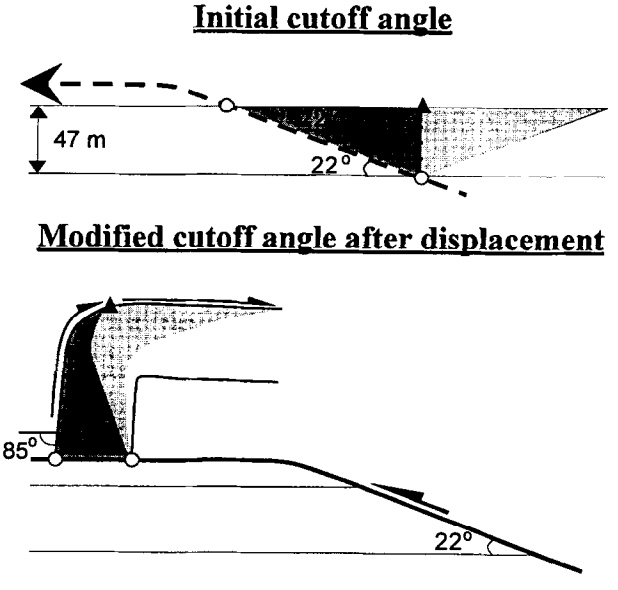

Fig. 5. Decrease in forelimb length by modification of hangingwall cutoff angle during thrust transport (medium gray — initial hangingwall wedge, light gray — equivalent mirror wedge in hangingwall to show rock displacement by cutoff modification, open circles — cutoffs for top and bottom of example, filled triangle — contact on upper layer boundary between the two wedges).

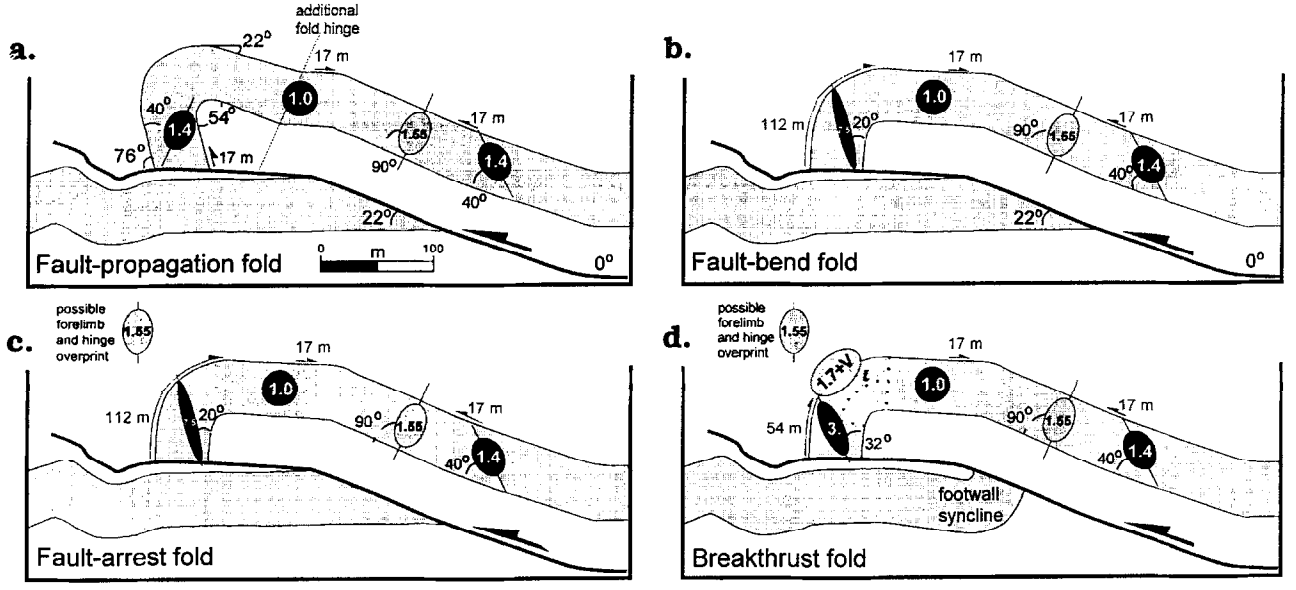

Fig. 6. Geometric comparisons to section BB′ (Fig. 3b) with kinematic predictions for different models of thrust-related folding. Black ellipses show flexural or intralayer flow, light gray ellipses show bending strains, thin slip arrows show flexural or interlayer slip with lengths equal to slip magnitude. Values calculated to nearest 0.05 for ellipse ratios and nearest meter for slip magnitudes for consistency with accuracy of field measurements.

and Medwedeff, 1990; Fischer *et al.*, 1992). The comparison of predicted distributions (Fig. 6) to microstructural distributions, mesostructural distributions, and measured strains from the field example will test model applicability to fold origin.

In quartz arenites at a relatively low temperature (Onasch, 1990; Wu and Groshong, 1991; Onasch and Dunne, 1993; Couzens and Dunne, 1994), deformation includes interlayer and flexural slip, intralayer and flexural flow, and bending (Fig. 6). These deformations were calculated where applicable for each model (Fig. 6), and the equations for the calculations were:

(1) flexural slip: $S = t\theta$ (eq. #7-38, Ramsay, 1967)

(2) interlayer slip (Fig. 5): $\text{slip} = \frac{t}{\tan\theta_o} - \frac{t}{\tan\theta_h}$

$$R = \left(2 + \gamma^2 + \gamma(\gamma^2 + 4)^{1/2}\right)/2$$

(3) flexural flow: $\tan 2\theta = 2/\gamma$

(eq.#21.7 & 21.8, Ramsay and Huber, 1987)

(4) simple shear: $\gamma = \tan\theta$ (p. 3, Ramsay and Huber, 1983)

(5) bending strain above fault bends: $\epsilon = \frac{t\theta_o\beta}{4}$

(eq. #3c, Wiltschko *et al.*, 1985)

(6) bending strain in other fold hinges: $\frac{L_2}{L_1} \times 100$,

where S is layer-parallel slip, t is mechanical layer thickness, θ is the dip of the layer, θ_o is the footwall cutoff angle, θ_h is the final hangingwall cutoff angle, γ is the shear strain, R is the aspect ratio of the finite strain ellipse, θ'' is the angle between the long axis of the finite strain ellipse and bedding, L_1 is the length of neutral surface in fold profile, L_2 is the length of the outer arc in fold profile, and $\beta = \pi/S_o$, where variable S_o is one-half of the arc length of the fault-bend fold at the top of the bending layer.

Figure 6 does not show the cumulative deformation for each model but rather a range of possible maximum deformations if single processes were active. For example, in the backlimb of the fault-bend fold (Fig. 6b), possible deformations include a layer-parallel slip of 17 m (equation 1), layer-parallel shear for a strain ratio of 1.4 with a long axis at 40° to bedding (equation 3), and bending through the lower fault bend of the footwall for a strain ellipse ratio of 1.55 (equation 5). If several behaviors were concurrent, deformation magnitudes for each would be smaller. Presumably, in a successful test the field data provide a basis for distinguishing which end-member or suite of deformations actually occurred.

All three models predict the same deformation in the backlimb because these rocks behave the same during passage over the footwall ramp (Fig. 6b–d). Thus, if a kinematic test is to distinguish among models, the deformation differences in the hinge and forelimb must be examined. Because the hangingwall cutoff angle changes from 22° to 85° (Fig. 5) for both fault-bend and fault-arrest fold models, much of their predicted deformation in the forelimb and hinge is the same (Fig. 6b & c). The predicted deformations for these two models in Fig. 6 were calculated by assuming that material passed through the hinge from the forelimb by some combination of slip and flow (Fig. 5). The fault-arrest model may record additional deformation such as bending strains

during passage over the upper bend of the footwall ramp because much of the fold formed prior to passage. Otherwise, it would be difficult to distinguish these two models kinematically.

A break-thrust origin yields a significantly different prediction. A post-folding thrust that transects layering with nearly a 90° cutoff angle in the forelimb and is parallel to layering in the backlimb produces the observed hangingwall cutoff angle (Fig. 6d). For such a cutoff angle, the forelimb dip would be 63° before thrust propagation. As a result, forelimb deformation is less than in the other two models because limb dip was smaller after fold growth. Also, deformation in the forelimb results from fold amplification and not from change in cutoff angle, as in the other two models. Thus, material is not required to pass from forelimb to hinge.

A break-thrust anticline might contain overprinting deformation from passage over the upper bend of the footwall. Fold shape is otherwise unmodified by passage through the upper bend because fault trajectory is assumed to be parallel to the backlimb dip. A geometric difference between the break-thrust model and the other two models is the requirement of a footwall syncline. Existing field data neither support nor preclude this possibility because no footwall rocks are exposed within 20 m of the Barclay thrust (Fig. 2).

To summarize, model predictions indicate a great deal of similarity between the fault-bend and fault-arrest models, but that a break-thrust fold will have different deformation intensities and no need for material migration through the anticlinal hinge. The kinematic predictions of these three models will be compared to field data to show that a kinematic test is sufficient to distinguish a unique origin for the Barclay anticline.

STRUCTURAL DISTRIBUTIONS AND STRAIN DATA

Mesostructural distribution

Mesoscale structures in the Tuscarora Sandstone of the study area include bed-parallel slip surfaces, contraction faults, contractional cataclastic bands and veins (Fig. 7). The forelimb and main hinge contain most mesostructures, whereas the backlimb exhibits few and they are absent in the footwall.

Bed-parallel slip surfaces with slickenlines in the forelimb terminate in the hinge, and are absent in the backlimb (Fig. 7a). They have an average separation of 2.9 m in the forelimb that decreases from 7.5 m to about 1 m as bedding dip increases. Pervasive contraction faults and cataclastic bands (Lloyd and Knipe, 1992; Onasch and Dunne, 1993) occur only in the basal pebble conglomerate of the forelimb and hinge inner-arc (Fig. 8a & c). They offset pebbles, exhibit slickenlines, and decrease to zero abundance at 6 m above the base of the Sandstone (Fig. 7b). They are spaced at 3.4 ± 3.0 cm intervals with widths of < 1 mm, have displacements of about 0.5 mm, and are approximately strike parallel with a variety of dips to the northwest (Fig. 8a).

The inner arc of the hinge along the northern section contains a unique fracture suite (Fig. 7c & Fig. 8). Four different fracture sets (Fig. 8b) are so abundant that the sandstone has a 'cookie-cutter' appearance with a block size of 2–3 cm that obscures bedding. Bedding is offset locally by contraction faults with dip-slip or oblique dip-slip slickenlines, but mostly bedding is obscured by the fracture intensity. This intense fracture abundance disappears outward in the hinge in just 5 m. The mesoscale strains from these fracture populations could not be determined due to an insufficient number of measurable offsets, slip directions and dilations (Jamison, 1989; Wojtal, 1989).

The intense fracture population in the northern hinge contrasts with the contraction faults and bed-parallel slip surfaces of the southern hinge and forelimb. This contrast is interpreted to represent a difference in hinge deformation during fold amplification. A major factor during development of hinge-related structures is fold hinge migration (Williams, 1979; Gray, 1981; Mitchell and Woodward, 1988; Fischer *et al.*, 1992). For example, tangential longitudinal strain forms structures in the hinge zone (Ramsay, 1967). If the hinge is fixed, a unique suite of structures develops there (Mitchell and Woodward, 1988; Fischer *et al.*, 1992). If the hinge migrates during folding, the suite would be found in the hinge and at least one fold limb because structures pass from hinge to limb (Williams, 1979; Gray, 1981; Fischer *et al.*, 1992). As a result, the distribution of contraction faults in forelimb and hinge with bed-parallel slip surfaces terminating in the hinge is interpreted to indicate hinge migration. However, the intense fracture population found only in the northern hinge indicates that this hinge was locally fixed at some point during fold amplification. In summary, localization of contraction faults and bed-parallel slip surfaces in hinge and forelimb indicates fold amplification by growth of the forelimb with some hinge pinning, rather than material transport from forelimb to backlimb via the hinge.

Microstructural distribution

The bed-perpendicular, strike-perpendicular thin-sections ('v' sections) of 42 samples were point-counted at 250 spots for microstructural abundance (Table A1 in Appendix 1, Fig. 7d–g) (Groshong, 1988; Houseknecht, 1988; Onasch, 1990; Wu and Groshong, 1991; Onasch and Dunne, 1993). Abundances were tabulated for five structural domains and for all samples (Table A1 in Appendix 1). Structures include: (1) undulatory extinction; (2) deformation lamellae (Fig. 7d); (3) deformation bands, (Fig. 7e); (4) fluid inclusion planes (FIPs) or healed microfractures (Fig. 7d); (5) quartz-filled transgranular microveins with widths of 0.01–0.20 mm, which have optical continuity with adjacent grains in trans-

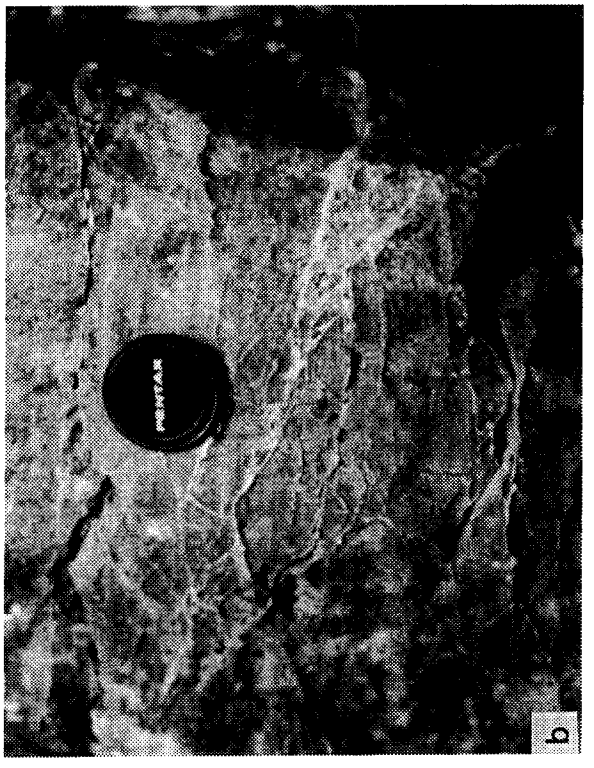

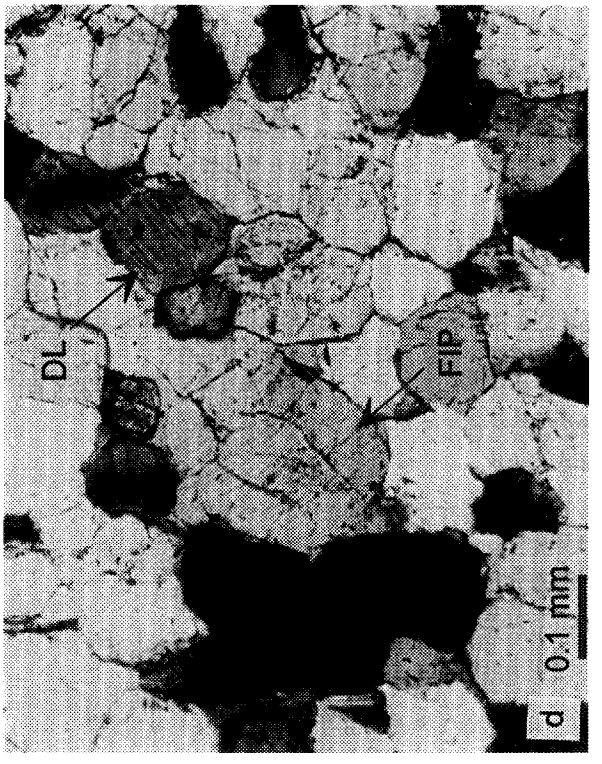

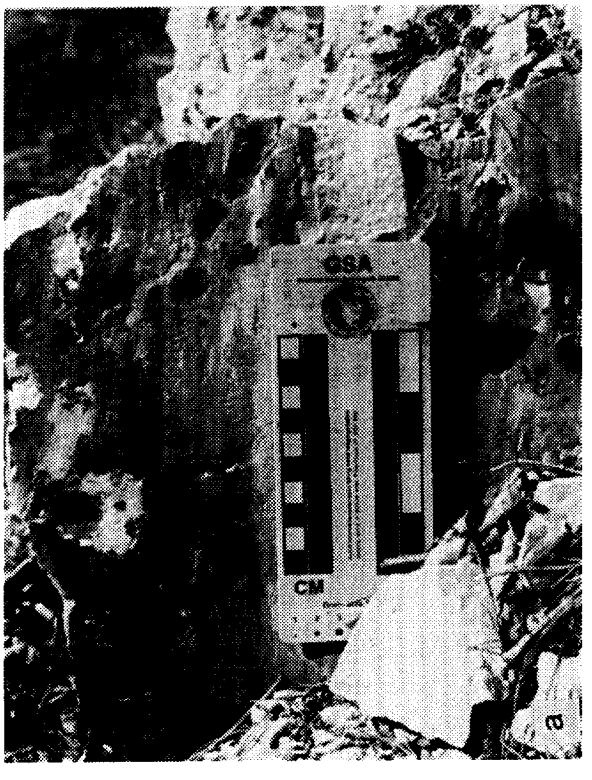

Fig. 7(a–d).

mitted light but are dull in cathodoluminescence (Fig. 7f); (6) subplanar transgranular cataclastic bands of fine-grained, poorly sorted angular quartz that offset adjacent quartz grains; (7) teeth-like transgranular stylolites with insoluble residues; and (8) interpenetrated grains are common in cathodoluminescence (Fig. 7g) and but could not be point-counted with the CL apparatus. Cathodoluminescence was also used to verify that structures such as FIPs, microveins and deformation lamellae were postdiagenetic. Cathodoluminescence distinguishes dull cements from pink and blue detrital grains. Microstructures that cut both detrital grains and cement are interpreted as post-diagenetic.

Undulatory extinction is the most common and uniformly distributed feature in all domains (Table A1 in Appendix 1). Deformation bands, deformation lamellae and FIPs are the next most abundant and are uniformly distributed. Microveins occur in all domains. Cataclastic bands, which are restricted to the basal conglomerate in forelimb and hinge (as are mesoscale cataclastic bands), are always accompanied by microveins. Stylolites are rare.

Relative age data for the microstructures are sparse, but a few consistent observations can be made. Microveins occur with parallel transgranular FIPs, suggesting that they are age-equivalent (Onasch, 1990). Microveins and cataclastic bands consistently cross-cut interpenetrated grains, indicating that grain-to-grain solution predated fracturing. Where multiple microvein sets occur together, they separate but do not offset each other, indicating coeval formation. Some microvein grains contain undulatory extinction, deformation lamellae and deformation bands, which means that some dislocation-related deformation postdated vein formation. In summary, most microstructures are distributed uniformly throughout the Barclay anticline, except for the restriction of cataclastic bands and microveins to hinge and forelimb.

Finite strain

For each thin section from all 42 samples, boundaries of 200 quartz grains were digitized to determine finite strain with the normalized Fry method (Fry, 1979; Erslev, 1988). Original detrital quartz grain boundaries were distinguished from optically continuous cement overgrowths using cathodoluminescence photomicrographs (Houseknecht, 1988). Detrital grains preserve their original grain centers, permitting the use of the quartz grains as strain markers (Dunne *et al.*, 1990). Strain ellipsoids were then calculated from the three mutually perpendicular strain ellipses of each sample (Owens, 1984).

Sample sites were chosen to eliminate transgranular heterogeneous structures, such as microveins and stylolites, so as to measure homogeneous strain at the scale of the 200-grain domains. Possible contributors to pervasive deformation based on abundance at this scale are dislocation-related structures and grain-to-grain solution features (Table A1 in Appendix 1, Fig. 7).

Flinn plots for R_{xy} and R_{yz} ratios (Fig. 9a–e) show no relationship between structural domain and strain magnitude. All domains record small strain ratios of mostly less than 1.25. These small ratios may represent the canceling effect of the two deformations believed to be prevalent in sandstones of the central Appalachians: sedimentary compaction and layer-parallel shortening (Geiser, 1974; Engelder, 1979a,b; Nickelsen, 1979; Ferrill and Dunne, 1989; Couzens *et al.*, 1993; Couzens and Dunne, 1994; Onasch, 1994). Considering the ideal case, pretectonic bed-normal diagenetic volume loss of 10–30% produces R_{yz} values of 1.11–1.43 (Fig. 9f) for R_{xy} values of about 1.00 (Ramsay and Wood, 1973). Regional LPS is normal to the compaction and reduces R_{yz} ratios while increasing R_{xy}, which keeps strain ratios small (Fig. 9f). Measured strain ratios fall within the predicted range and some plots have data points distributed along a line of negative slope as in Fig. 9(f).

Finite-strain ellipsoid axial orientations are depicted with bedding rotated to the horizontal, a convenient common reference frame when considering compaction and LPS (Fig. 10). Z-axes cluster about the bedding normal and X- and Y-axes for the four hangingwall domains show bedding girdles (Fig. 10). These geometries are consistent with deformation dominated by layer-normal shortening, such as pretectonic diagenetic compaction (Couzens *et al.*, 1993). The combination of small strain ratios, some data distributions with negative slopes in Flinn plots, and the clustering of Z-axes are interpreted to indicate a deformation history dominated by compaction rather tectonic shortening.

Grain-to-grain solution strain

Volume loss due to grain-to-grain solution was determined for a representative sample set using a new pressure solution strain (PSS) method (Onasch, 1993, 1994). The method determines strain from the magnitudes of quartz grain interpenetrations (Houseknecht, 1988; Onasch, 1993), which are visible in cathodoluminescence but not transmitted-light photomicrographs (Fig. 7g & h). Only 20 samples were analyzed (Table A2

Fig. 7. Mesostructures: (a) bedding-parallel slip surfaces in steeply dipping Tuscarora Sandstone; (b) cataclastic bands in basal pebble conglomerate of southern hinge (lens cap is 5 cm in diameter); and (c) fracturing in northern hinge (white lines approximate bedding orientation; length of photo represents approximately 6 m). Microstructures: (d) deformation lamellae (DL) and fluid inclusion planes (FIP) viewed under crossed polarizers; (e) deformation bands (DB) viewed under crossed polarizers; (f) microvein (MV) viewed under cathodoluminescence (CL); Grain-to-grain solution: (g) CL photomicrograph of grain-to-grain interpenetrations (original grain boundaries noted by black lines); (h) same view as (g), but under crossed polarizers.

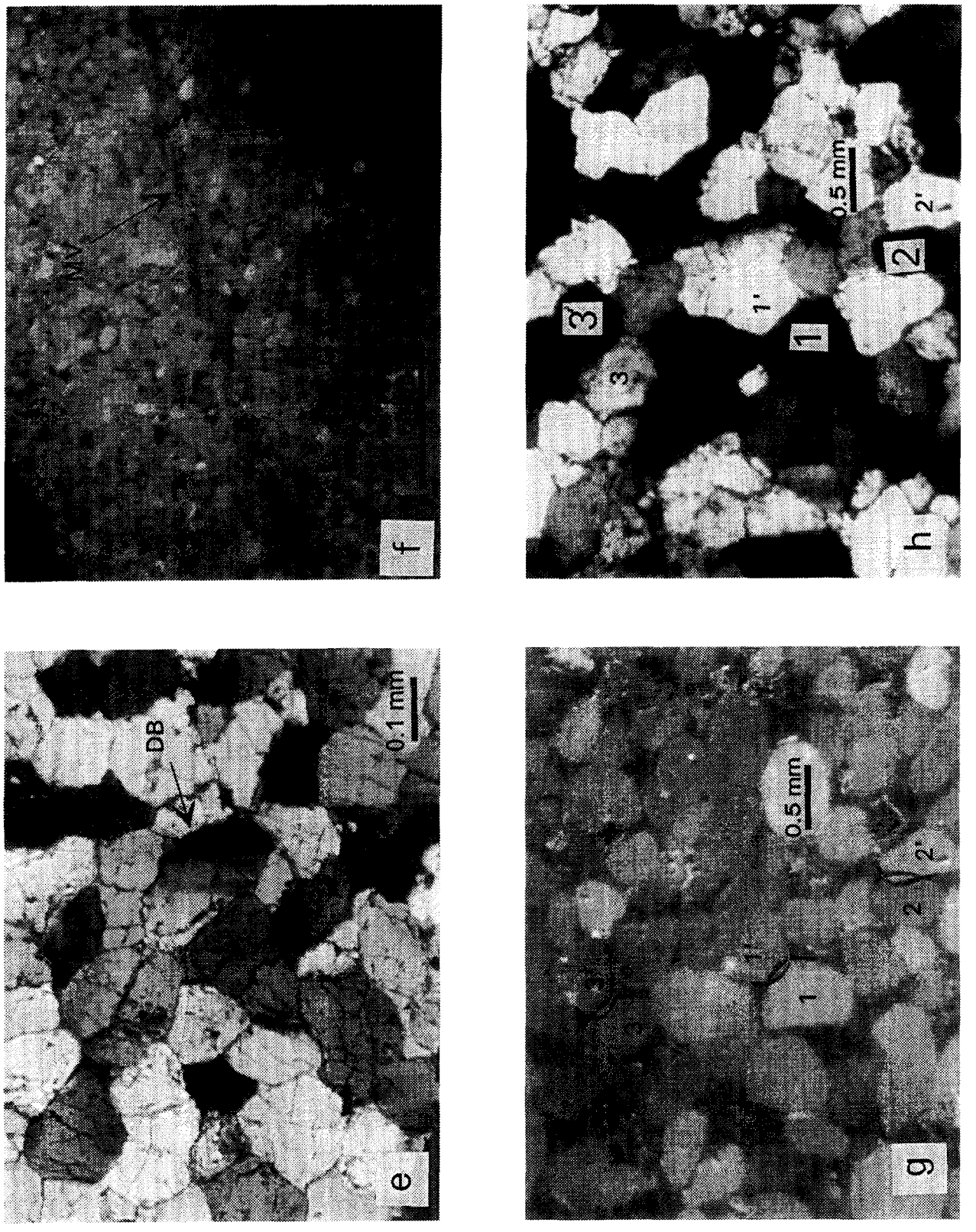

Fig. 7(e–h).

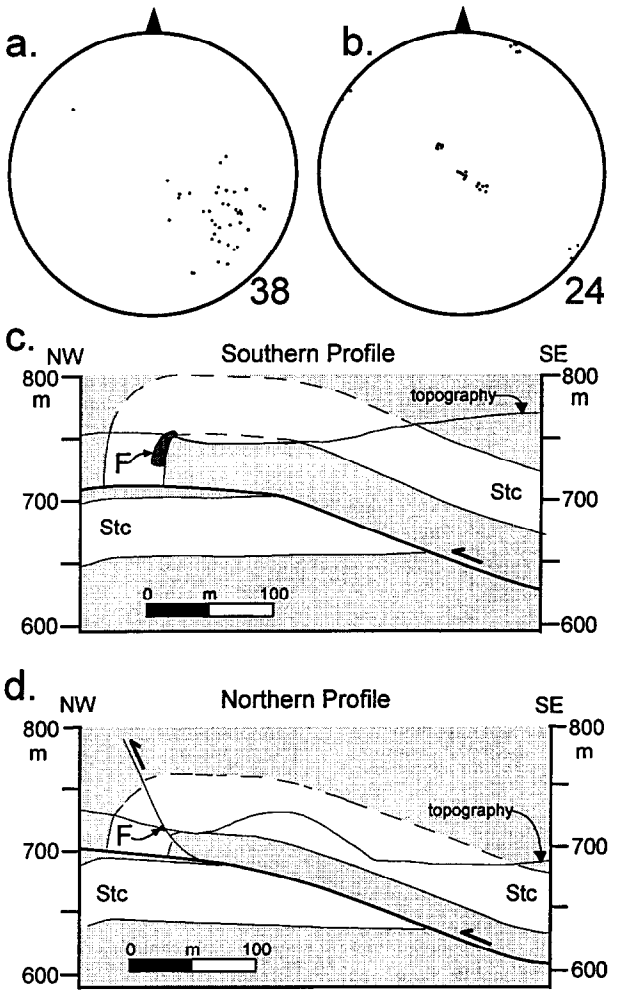

Fig. 8. (a) Equal-area lower-hemisphere stereonet for fault population in northwest limb of anticline in southern profile. (b) Equal-area lower-hemisphere stereonet for fracture population in hinge of northern profile. (c) Location of exposed faults (shaded area with F label) in northwest limb of southern profile. (d) Location of exposed fractures (shaded area with F label) in hinge of northern profile.

in Appendix 2) because the PSS method is quite time consuming, and homogeneously deformed regions were selected again.

R_{xy} and R_{yz} ratios are small with most less than 1.05 (Fig. 11), so calculated ellipsoids are nearly spherical. Yet, the elongations from volume loss are significant, ranging from 10 to 20% (Table A2 in Appendix 2). Consequently, average area loss is 27% per thin section and average volume loss per sample is $28 \pm 3\%$ by solution (Table A2 in Appendix 2). The average volume loss of 28% from PSS is greater than the combined rock porosity ($< 1\%$), average amount of preserved diagenetic cement (6%), and positive dilations from microvein formation ($\leq 9.5\%$). Therefore, the Tuscarora Sandstone underwent net volume loss during lithification and tectonism.

PSS ellipsoid axis orientations are depicted in equal-area stereonets where bedding was rotated to the horizontal (Fig. 12). The PSS ellipsoid axes for the Tuscarora Sandstone display no polar or girdle distributions (Fig. 12), reflecting the nearly spherical ellipsoid shapes.

The lack of a compaction imprint in PSS data may be explained by sources of error for this measurement technique. Onasch (1993) showed that shortening normal to bedding during diagenesis is over-estimated, which is one error source. Examination of figs 6(a) and 8(a & c) in Onasch (1993) also shows that while shortening should be zero parallel to bedding during diagenetic compaction, the packing of a pre-existing grain fabric creates an apparent bed-parallel shortening of 5–15%. Thus, bed-normal shortening of up to 20% produces near circular strain ellipses because of pre-existing grain fabric. We interpret the near-spherical ellipsoids from the PSS method to result from compaction strain masked by the effects of a pre-existing grain fabric on the measurement technique.

Summary of strain results

The most important result from the strain measurements is that at the scale of 200-grain domains, deformation is uniformly distributed, compaction-dominated and small. The Tuscarora Sandstone records neither the bending strains in the backlimb and anticlinal hinge, nor the layer-parallel shears predicted by the models for thrust-related folding (Fig. 6).

DISCUSSION

Comparison of kinematic data to models

Actual microstructural distributions and strains do not correlate with the kinematic predictions of the three surviving models: fault-bend, fault arrest, and break-thrust folding (Fig. 6). Instead, the small measured strains are the result of ubiquitous dislocation-related structures and grain-to-grain solution features that mostly accommodated deformation prior to fold–thrust development. As pervasive continuous microscale deformation does not account for the formation of the Barclay anticline, it is the geometry and distribution of the slip-related mesostructures that constrain the determination of fold origin.

Considering layer-parallel slip, substantial material is transported from the forelimb through the hinge in the fault-bend and fault-arrest models (Figs 5 & 6b & c). Although bed-parallel slip surfaces are abundant in the forelimb of the Barclay anticline, they terminate in the hinge and are absent in the backlimb. Also, contraction faults are present only at the base of the Tuscarora Sandstone and are absent in the backlimb. This mesostructural distribution precludes material transport through the hinge from the forelimb. Fault-bend and fault-arrest models, therefore, cannot be used to explain the origin of the Barclay anticline.

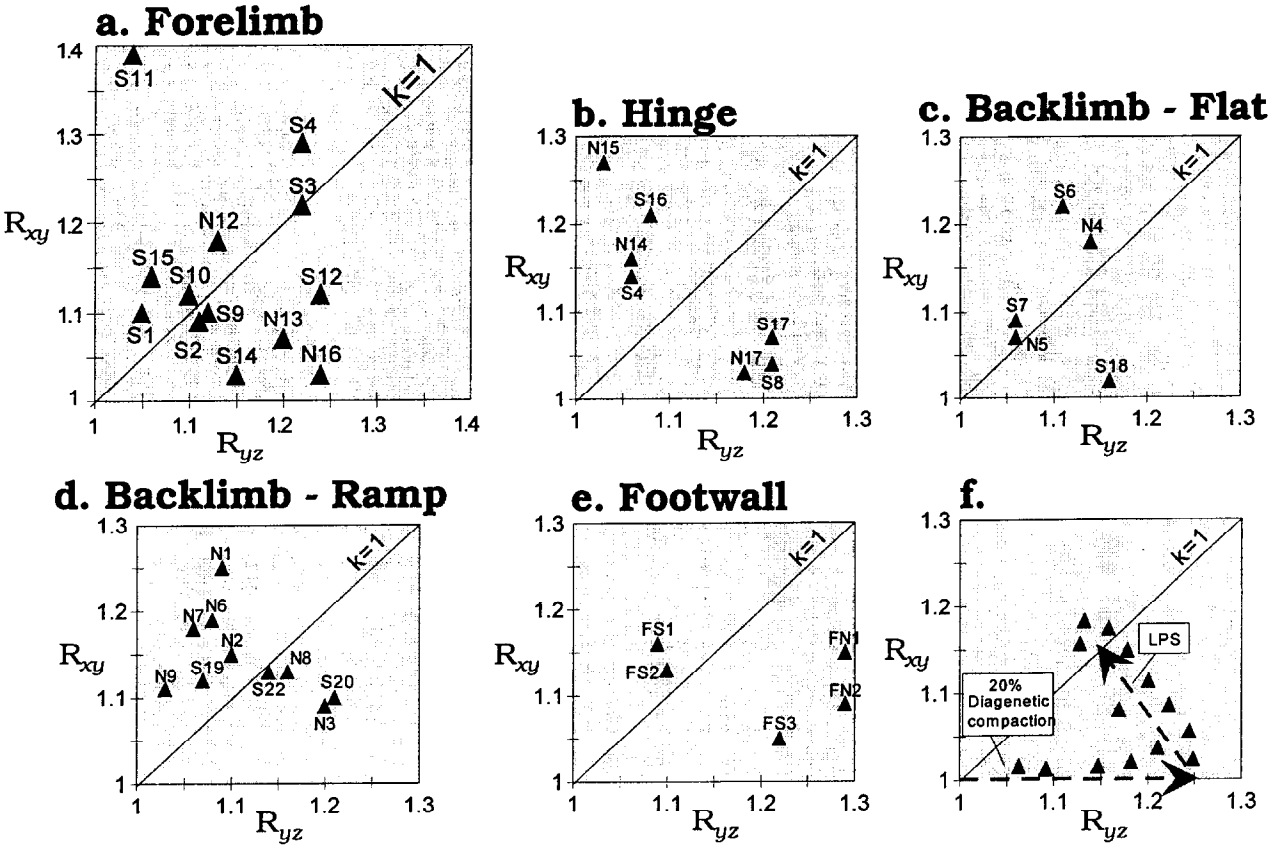

Fig. 9. (a)–(c) Flinn plots of finite strain data by structural domains. (f) Theoretical Flinn plot for a two-step deformation of bed-normal compaction followed by layer-parallel shortening.

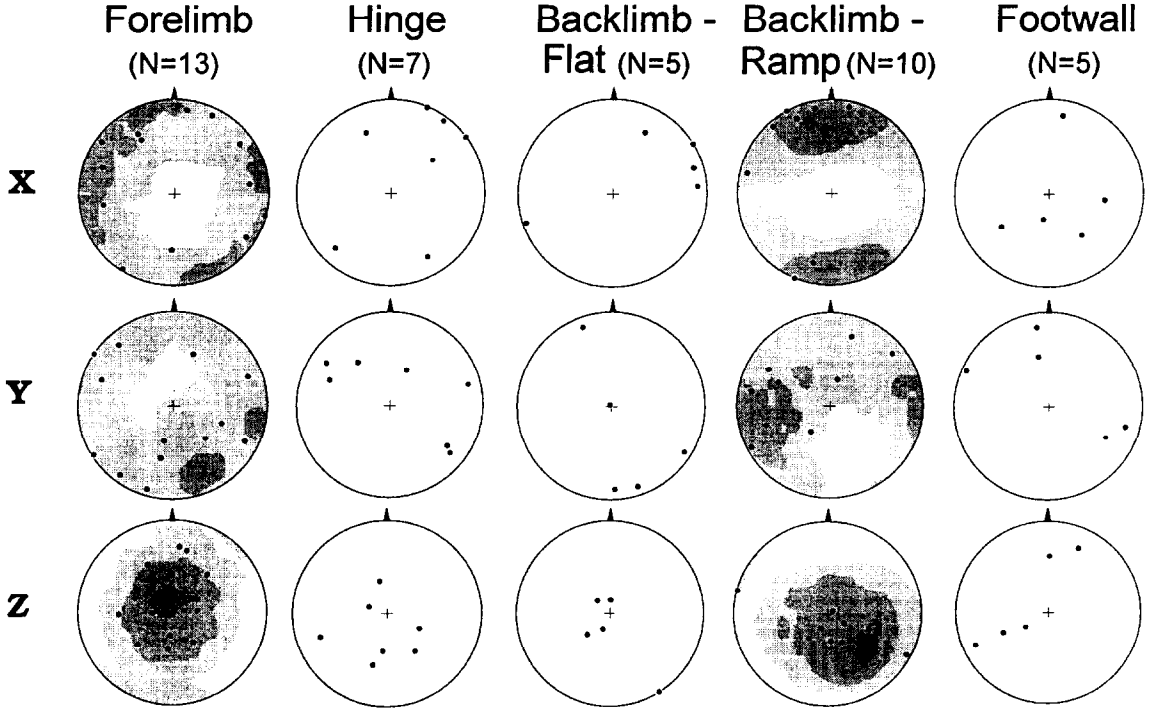

Fig. 10. Equal-area lower-hemisphere stereonets for orientations of ellipsoidal strain axes for the finite strain data. (u) — in present day orientation, (r) — with bedding restored to the horizontal, N values — number of stations, and where present, contoured by Kamb (1959) method for a 3σ interval.

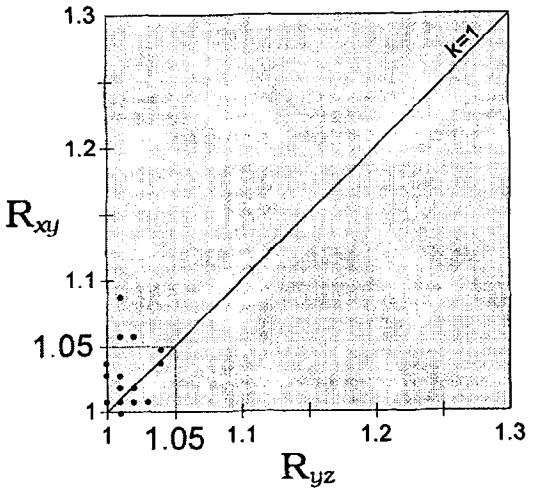

Fig. 11. Flinn plot for PSS strain data. Graph scaled to 1.3 for comparison to Fig. 10.

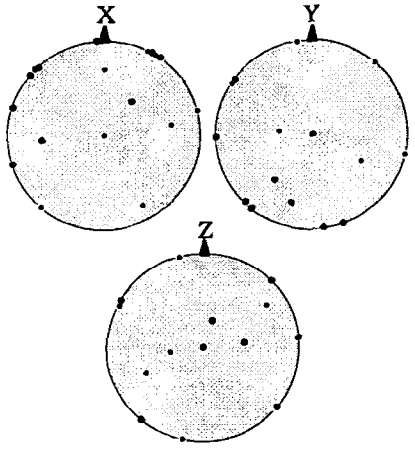

Fig. 12. Equal-area lower-hemisphere stereonets with bedding restored to the horizontal at all stations to show the orientations of the ellipsoidal strain axes for the PSS data. Where number of points in a plot is less than 'N', 'missing' points are coincident on center point.

The distribution of bed-parallel slip surfaces is consistent with flexural slip (Ramsay, 1967), except in the backlimb. The absence of slip surfaces in the backlimb may indicate that the anticline developed as a kink fold with one active limb (Stewart and Alvarez, 1991). However, the small slip amounts required for the gently dipping southeastern limb may have been absorbed within the two weak racetrack layers of the Tuscarora Sandstone. Flexural-slip dominated folding explains the paucity of microstructural evidence for bending strain in the anticlinal hinge. The only mesoscale evidence for bending are the contraction faults in the inner arcs of both profiles. The faults in the basal conglomerate of the south profile record small deformations and are present in both the forelimb and hinge. They are interpreted to have formed in the hinge and to have moved into the forelimb as the hinge migrated into the backlimb. The greater deformation in the northern exposure of the hinge is interpreted to result from hinge pinning during fold amplification. These interpretations, together with the lack of evidence for outer-arc extension in the anticlinal hinge, indicate that bending was not operative at the mesoscale. Bed-parallel slip, perhaps during kinking, with negligible bending deformation in the hinge may be explained by break-thrusting (Fig. 6d).

For a break-thrust origin, folding preceded thrust propagation and was achieved by layer-parallel slip in the forelimb, contraction faulting in the hinge, hinge migration with local pinning, and possibly kink-folding (Fig. 13a). For this explanation, fold asymmetry may result from a local propensity for bed-parallel slip (Chapple and Spang, 1974; Stewart and Alvarez, 1991). The syncline shown in Fig. 13 is not precluded by the existing data because of the 130 m exposure gap between footwall and hangingwall (Fig. 2).

The anticline would then displace without significant modification during thrust displacement, if the fault exploited bedding where possible during propagation (Fig. 13b). This explanation is consistent with both the geometric and kinematic constraints preserved within exposures of the Barclay anticline. Kinematic analysis was necessary to reduce the number of possible origins for the thrust-related fold from three to one. Geometric testing alone could not achieve this objective.

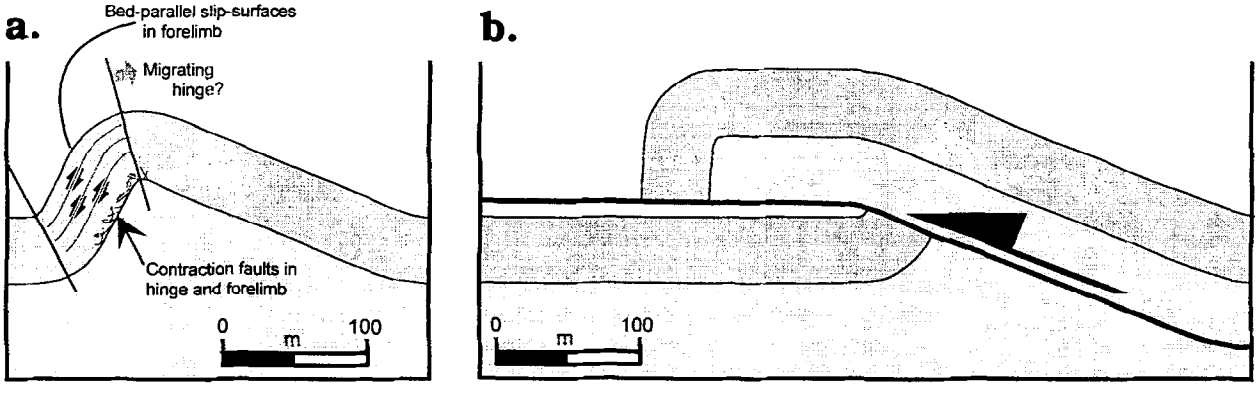

Fig. 13. Proposed deformation history for the Barclay anticline, using section BB' as a template.

Another problem for geometric tests

This study has shown that geometric tests for the origin of fold–thrust combinations are insufficient because more than one model may accommodate the known field geometry. Another problem for geometric tests is the accuracy of the necessary geometric measurements. Geometric tests commonly compare parameters such as fault dip, interlimb angle, unit thickness, and bed length to determine applicability of a model with great precision (Suppe, 1983; Jamison, 1987; Mitra, 1990; Suppe and Medwedeff, 1990; Homza and Wallace, 1995). However, the precision of this approach may be subverted by the accuracy of the available measurements in real geological examples. Consider a thrust-related fold with a steeply dipping forelimb and two more likely situations when such a structure is examined: (1) seismic reflection data where the steeply dipping forelimb is poorly imaged and all vertical information is initially in time and not distance units; and (2) a moderately forested terrain with a temperate moist climate where erosion prevents complete exposure of rock layers and accurate thickness measurements. In these two situations, it could easily be impossible to resolve unit thicknesses accurately. If the error for thickness measurement is 25% (a conservative value in both of these situations), several models could explain fold origin. For example, consider applying this 25% error to the plots of Fig. 4. The light gray fields in this figure show the regions where values for pairs of angles (e.g. ramp angle, fold interlimb angle, backlimb dip) may be explained by either a thickness measurement in the modeled fold or a 25% smaller thickness measurement in the same location within a fault-propagation fold. Examining the location of the stippled fields in the graphs, the possibility of more than one origin from geometric tests is particularly prevalent when initial thrust dip is 30° or less, a common situation.

These models of kinematic origin for fault-related folds have the important convenience of yielding reproducible results even where data are poor. Still, we hope that in future discussions of thrust-related folds and their cross-sections, workers will consider measurement accuracy when applying geometric tests to determine origin.

CONCLUSIONS

(1) Geometric tests could not uniquely elucidate the origin of the Barclay anticline because more than one model matched the field geometry. A kinematic test with micro- and mesoscale data was necessary to reduce the number of admissible solutions to one.

(2) The Barclay anticline is interpreted to result from break-thrusting with hinge migration prior to offset by a propagating thrust. Previously, workers have interpreted that break-thrust folds form with fixed hinges (Mitchell and Woodward, 1988; Fischer *et al.*, 1992). As break-thrust folds precede thrusting, the structures should be free to grow by any mechanism of natural folding (e.g. Nickelsen, 1979; Gray, 1981; Stewart and Alvarez, 1991). Therefore, a fixed hinge is not a requirement for a break-thrust fold.

(3) Pervasive microscale deformation did not contribute significantly to the formation of the Barclay anticline. Although time-consuming, measurement of deformation at this scale is necessary to prevent false application of kinematic models, particularly in limestones or coarse clastic rocks with clay matrix, which may contain significant microscale deformation (e.g. Geiser, 1974; Marshak and Engelder, 1985; Ferrill and Dunne, 1989; Protzman and Mitra, 1990).

(4) As a cautionary note, users of geometric tests for thrust-related folds are encouraged to assess measurement accuracy as a verification of uniqueness of result.

Acknowledgements—This work was partially funded by NSF grant EAR-9206617 to Dunne, and by grants-in-aid from the Geological Society of America, the American Association of Petroleum Geologists and Sigma Xi to Thorbjornsen. We would like to thank R. Hatcher Jr. and S. Driese for comments to an earlier version, and Mary Beth Gray and an anonymous reviewer for their comments. Kevin Smart and Robert Fisher are thanked for field assistance.

REFERENCES

Al Saffar, A. (1993) Geometry of fault-propagation folds; method and application. *Tectonophysics* **223**, 363–380.

Alonso, J. L. and Teixell, A. (1992) Forelimb deformation in some natural examples of fault-propagation folds. In *Thrust Tectonics*, ed. K. R. McClay, pp. 175–180. Chapman and Hall, New York.

Armstrong, P. A. and Bartley, J. M. (1993) Displacement and deformation associated with a lateral thrust termination, southern Golden Gate Range, southern Nevada, U.S.A. *Journal of Structural Geology* **15**, 721–736.

Bambach, R. K. (1987) The Ordovician–Silurian unconformity in western Virginia and adjacent West Virginia. *Appalachian Basin Industrial Associates* **13**, 2–14.

Butler, R. W. H. (1992) Structural evolution of the western Chartreuse fold and thrust system, NW French Subalpine Chains. In *Thrust Tectonics*, ed. K. R. McClay, pp. 287–297. Chapman and Hall, New York.

Cecil, C. B. (1972) General geology of the Browns Mountain anticline, southeastern West Virginia. In *Appalachian Structures: Origin, Evolution, and Possible Potential for New Exploration Frontiers*, eds P. Lessing, R. I. Hayhurst, J. A. Barlow and L. D. Woodfork, pp. 181–193. West Virginia University and West Virginia Geological and Economic Survey.

Cello, G., Tortorici, L., Martini, N. and Paltrinieri, W. (1989) Structural styles in the frontal zones of the southern Apennines, Italy: An example from the Molise District. *Tectonics* **8**, 753–768.

Chapman, T. J. and Williams, G. D. (1984) Displacement–distance methods in the analysis of fold–thrust structures and linked-fault systems. *Journal of the Geological Society, London* **141**, 121–128.

Chapple, W. M. and Spang, J. H. (1974) Significance of layer-parallel slip during folding of layered sedimentary rocks. *Geological Society of America Bulletin* **85**, 1523–1534.

Chen, P. (1981) Lower Paleozoic stratigraphy, tectonics, paleogeography, and oil/gas possibilities in the central appalachians (West Virginia and adjacent states)—Part 2, Measured sections. *West Virginia Geology and Economic Survey Report Investigation* **26**.

Colton, G. W. (1970) The Appalachian basin — Its depositional sequences and their geologic relationships. In *Studies of Appalachian Geology: Central and Southern*, eds G. W. Fisher, F. J. Pettijohn, J. C. Read, Jr and K. N. Weaver, pp. 5 47. Wiley–Interscience, New York.

Cooper, M. A., Garton, M. R. and Hossack, J. R. (1983) The origin of

the Basse Normadie duplex, Boulonnais, France. *Journal of Structural Geology* **5**, 139–151.

Couzens, B. A., Dunne, W. M., Onasch, C. M. and Glass, R. (1993) Strain transition at the juncture of two diachronous thrust systems: Southern vs central Appalachian foreland. *Journal of Structural Geology* **15**, 451–463.

Couzens, B. A. and Dunne, W. M. (1994) Displacement transfer at thrust terminations: Saltville thrust and Sinking Creek anticline, Virginia, U.S.A. *Journal of Structural Geology* **16**, 781–793.

Dahlstrom, C. D. A. (1990) Geometric constraints derived from the law of conservation of volume and applied to evolutionary models of detachment folding. *Bulletin of the American Association of Petroleum Geologists* **74**, 336–344.

Dominic, J. and McConnell, D.A. (1994) The influence of structural lithic units in fault-related folds, Seminoe Mountains, Wyoming, U.S.A. *Journal of Structural Geology* **16**, 769–779.

Dorsch, J., Bambach, R. K. and Driese, S. G. (1994) Basin-rebound origin for the 'Tuscarora Unconformity' in southwestern Virginia and its bearing on the nature of the Taconic orogeny. *American Journal of Science* **294**, 237–255.

Dunne, W. M., Onasch, C. M. and Williams, R. (1990) The problem of strain-marker centers and the Fry method. *Journal of Structural Geology* **12**, 933–938.

Engelder, T. (1979) Mechanisms for strain within the Upper Devonian clastic sequence of the Appalachian plateau, western New York. *American Journal of Science* **279**, 527–542.

Engelder, T. (1979) The nature of deformation within the outer limits of the central Appalachian foreland fold and thrust belt in New York State. *Tectonophysics* **55**, 289–310.

Erslev, E. A. (1988) Normalized center-to-center strain analysis of packed aggregates. *Journal of Structural Geology* **10**, 201–209.

Erslev, E. (1991) Trishear fault-propagation folding. *Geology* **19**, 617–620.

Ferrill, D. A. and Dunne, W. M. (1989) Cover deformation above a blind duplex: an example from West Virginia, U.S.A. *Journal of Structural Geology* **11**, 421–431.

Fischer, M. P., Woodward, N. B. and Mitchell, M. M. (1992) The kinematics of break-thrust folds. *Journal of Structural Geology* **14**, 451–460.

Fisher, D. M. and Anastasio, D. J. (1994) Kinematic analysis of a large-scale leading edge fold, Lost River Range, Idaho. *Journal of Structural Geology* **16**, 337–354.

Fry, N. (1979) Random point distributions and strain measurement in rocks. *Tectonophysics* **60**, 89–105.

Geiser, P. A. (1974) Cleavage in some sedimentary rocks of the central Valley and Ridge Province, Maryland. *Geological Society of America Bulletin* **85**, 1399–1412.

Gray, D. R. (1981) Cleavage–fold relationships and their implications for transected folds: an example from central Virginia. *Journal of Structural Geology* **3**, 265–277.

Groshong, R. H. (1988) Low temperature deformation mechanisms and their interpretation. *Geological Society of America Bulletin* **100**, 1329–1360.

Groshong, R. H. and Epard, J.-L. (1994) The role of strain in area-constant detachment folding. *Journal of Structural Geology* **16**, 613–618.

Hardy, S. and Poblet, J. (1994) Geometric and numerical model of progressive limb rotation in detachment folds. *Geology* **22**, 371–374.

Harris, A. G. (1979) Conodont color alteration, an organo–mineral metamorphic index, and its applications to Appalachian basin geology. In *Aspects of Diagenesis*, eds P. A. Scholle and P. R. Schulgar. Society of Economic Paleontologists and Mineralogists Special Paper **26**, 3–16.

Hedlund, C. A., Anastasio, D. J. and Fisher, D. M. (1994) Kinematics of fault-related folding in a duplex, Lost River Range, Idaho, U.S.A. *Journal of Structural Geology* **16**, 571–584.

Heim, A. (1921) *Geologie der Schweiz*. Tauchnitz, Leipzig.

Hennings, P. H. (1994) Structural transect of the southern Chihuahua Fold Belt between Ojinaga and Aldama, Chihuahua, Mexico. *Tectonics* **13**, 1445–1460.

Hippolyte, J. C., Angelier, J., Roure, F. and Casero, P. (1994) Piggyback basin development and thrust belt evolution: structural and palaeostress analyses of Plio-Quarternary basins in the southern Apennines. *Journal of Structural Geology* **16**, 159–173.

Homza, T. X. and Wallace, W. K. (1995) Geometric and kinematic models for detachment folds with fixed and variable detachment depths. *Journal of Structural Geology* **17**, 575–587.

Houseknecht, D. W. (1988) Intergranular pressure solution in four quartzose sandstones. *Journal of Sedimentay Petrology* **58**, 228–246.

Jadoon, I.A.K., Lawrence, R.D. and Lillie, R.J. (1994) Seismic data, geometry, evolution, and shortening in the active Sulaiman fold-and-thrust belt of Pakistan, southwest of the Himalayas. *Bulletin of the American Association of Petroleum Geologists* **78**, 758–774.

Jamison, W. R. (1987) Geometric analysis of fold development in overthrust terranes. *Journal of Structural Geology* **9**, 207–219.

Jamison, W. R. (1989) Fault–fracture strain in Wingate Sandstone. *Journal of Structural Geology* **11**, 959–973.

Jamison, W. R. (1992). Stress controls on fold thrust style. In *Thrust Tectonics*, ed. K. R. McClay, pp. 155–164. Chapman and Hall, New York.

Kamb, W. B. (1959) Ice petrofabric observations from Blue Glacier, Washington, in relation to theory and experiment. *Journal of geophysical Research* **64**, 1891–1909.

Kilsdonk, B. and Wiltschko, D. V. (1988) Deformation mechanisms in the southeastern ramp region of the Pine Mountain block, Tennessee. *Geological Society of America Bulletin* **100**, 653–664.

Kulander, B. R. (1968). A structural analysis of Browns Mountain anticline in West Virginia, Unpublished Ph.D. Thesis, West Virginia University.

Kulander, B. R., Dean, S. L. and Lessing, P. (1986) The Browns Mountain anticlinorium, West Virginia. *Geological Society of America Centennial Field Guide—Southeastern Section*, **6**, 101–104.

Laubscher, H. P. (1976) Fold development in the Jura. *Tectonophysics* **37**, 337–362.

Lloyd, G. E. and Knipe, R. J. (1992) Deformation mechanism accommodating faulting of quartzite under upper crustal conditions. *Journal of Structural Geology* **14**, 127–143.

Marshak, S. and Engelder, T. (1985) Development of cleavage in limestones of a fold–thrust belt in eastern New York. *Journal of Structural Geology* **7**, 345–359.

McConnell, D. A. (1994) Fixed-hinge, basement-involved fault-propagation folds, Wyoming. *Bulletin of the American Association of Petroleum Geologists* **77**, 1583–1593.

McDougall, J. W. and Hussain, A. (1991) Fold and thrust propagation in the western Himalaya based on a balanced cross section of the Surghar Range and Kohat Plateau, Pakistan. *Bulletin of the American Association of Petroleum Geologists* **75**, 463–478.

McNaught, M. A. and Mitra, G. (1993) A kinematic model for the origin of footwall syncline. *Journal of Structural Geology* **15**, 805–808.

Medwedeff, D. A. (1992) Geometry and kinematics of an active, laterally propagating wedge thrust, Wheeler Ridge, California. In *Structural Geology of Fold and Thrust Belts*, eds S. Mitra and G. Fisher, pp. 3–28. The Johns Hopkins Studies in Earth and Space Sciences, **5**.

Mitchell, M. M. and Woodward, N. B. (1988) Kink detachment fold in the southwest Montana fold and thrust belt. *Geology* **16**, 162–165.

Mitra, S. (1990) Fault-propagation folds: Geometry, kinematic evolution, and hydrocarbon traps. *Bulletin of the American Association of Petroleum Geologists* **74**, 921–945.

Mitra, S. and Namson, J. S. (1989) Equal-area balancing. *American Journal of Science* **289**, 563–599.

Morley, C. K. (1994) Fold-generated imbricates: examples from the Caledonides of Southern Norway. *Journal of Structural Geology* **16**, 619–631.

Mountjoy, E.W. (1992) Significance of rotated folds and thrust faults, Alberta Rocky Mountains. In *Structural Geology of Fold and Thrust Belts*, eds S. Mitra and G. Fisher, pp. 207–224. The Johns Hopkins Studies in Earth and Space Sciences, **5**.

Moustafa, A. R. and Khalil, S. M. (1995) Rejuvenation of the Tehyan passive continental margin of northern Sinai; deformation style and age (Gebel Yelleq area). *Tectonophysics* **241**, 225–238.

Narr, W. and Suppe, J. (1994) Kinematics of basement-involved compressive structures. *American Journal of Science* **294**, 802–860.

Nickelsen, R. P. (1979) Sequence of structural stages of the Alleghany orogeny, at the Bear Valley strip mine, Shamokin, Pennsylvania. *American Journal of Science* **279**, 225–271.

Onasch, C. M. (1990) Microfractures and their role in deformation of a quartz arenite from the central Appalachian foreland. *Journal of Structural Geology* **12**, 883–894.

Onasch, C. M. (1993) Determination of pressure solution shortening in sandstones. *Tectonophysics* **227**, 145–159.

Onasch, C. M. (1994) Assessing brittle volume-gain and pressure

solution volume-loss processes in quartz arenite. *Journal of Structural Geology* **16**, 519–530.
Onasch, C. M. and Dunne, W. M. (1993) Variation in quartz arenite deformation mechanisms between a roof sequence and duplexes. *Journal of Structural Geology* **15**, 465–475.
Owens, W. H. (1984) The calculation of a best-fit ellipsoid from elliptical sections on arbitrarily oriented planes. *Journal of Structural Geology* **6**, 571–577.
Parfenov, L. M., Prokopiev, A. V. and Gaiduk, V. V. (1995) Cretaceous frontal thrusts of the Verkhoyansk fold belt, eastern Siberia. *Tectonics* **14**, 342–358.
Passchier, C. W., Trouw, R. A., Zwart, H. J. and Vissers, R. L. M. (1992) Porphyroblast rotation: *eppur si muove*? *Journal of Metamorphic Geology* **10**, 283–294.
Protzman, G. M. and Mitra, G. (1990) Strain fabric associated with the Meade thrust sheet: implications for cross-section balancing. *Journal of Structural Geology* **12**, 403–417.
Ramsay, J. G. (1967) *Folding and Fracturing of Rock*. McGraw-Hill, New York.
Ramsay, J. G. (1992) Some geometric problems of ramp-flat thrust models. In *Thrust Tectonics*, ed. K. R. McClay, pp. 191–200. Chapman and Hall, New York.
Ramsay, J. G. and Huber, M. I. (1983) *The Techniques of Modern Structural Geology, Volume 1: Strain Analysis*. Academic Press, London.
Ramsay, J. G. and Huber, M. I. (1987) *The Techniques of Modern Structural Geology, Volume 2: Folds and Fractures*, Academic Press, London.
Ramsay, J. G. and Wood, D. S. (1973) The geometric ef fects of volume change during deformation processes. *Tectonophysics* **30**, 35–54.
Reger, D. B. (1931) Randolph County. *West Virginia Geology and Economic Survey, Morgantown, West Virginia.*
Reger, D. B. and Price, P. (1926) Mercer, Monroe, and Summers Counties. *West Virginia Geology and Economic Survey, Morgantown, West Virginia.*
Rich, J. L. (1934) Mechanics of low-angle overthrust faulting as illustrated by Cumberland thrust block, Virginia, Kentucky, and Tennessee. *Bulletin of the American Association of Petroleum Geologists* **18**, 1584–1596.
Schelling, D. and Arita, K. (1991) Thrust tectonics, crustal shortening, and the structure of the far-eastern Nepal Himalaya. *Tectonics* **10**, 851–862.
Schmidt, C. J., Genovese, P. W. and Chase, R. B. (1993) role of basement fabric and cover-rock lithology on the geometry and kinematics of twelve folds in the Rocky Mountain foreland. In *Laramide Basement Deformation in the Rocky Mountain Foreland of the Western United States*, eds C. J. Schmidt, R. B. Chase and E. A. Erslev, pp. 1–44. Special Paper of the Geological Society of America **280**.
Srivastava, P. and Mitra, G. (1994) Thrust geometries and deep structure of the outer and lesser Himalaya, Kumaon and Garhwal (India): Implications for evolution of the Himalayan fold-and-thrust belt. *Tectonics* **13**, 89–109.
Stewart, K. G. and Alvarez, W. (1991) Mobile-hinge kinking in layered rocks and models. *Journal of Structural Geology* **13**, 243–259.
Suppe, J. (1983) Geometry and kinematics of fault-bend folding. *American Journal of Science* **283**, 684–721.
Suppe, J., Chou, G. T. and Hook, S. C. (1992) Rates of folding and faulting determined from growth strata. In *Thrust Tectonics*, ed. K. R. McClay, pp. 105–122. Chapman and Hall, New York.
Suppe, J. and Medwedeff, D. A. (1990) Geometry and kinematics of fault propagation folding. *Eclogae Geologicae Helvetiae* **83**, 409–454.
Tavarnelli, E. (1994) Map analysis techniques and fold kinematics in the Umbrian Apennines. *Eclogae Geologicae Helvetiae* **87**, 33–46.
Wickham, J. (1995) Fault displacement-gradient folds and the structure at Lost Hills, California (U.S.A.). *Journal of Structural Geology* **17**, 1293–1302.
Williams, P. F. (1979) The development of asymmetrical folds in a cross-laminated siltstone. *Journal of Structural Geology* **1**, 19–30.
Williams, G. and Chapman, T. (1983) Strains developed in the hanging walls of thrusts due to their slip-propagation rate: a dislocation model. *Journal of Structural Geology* **5**, 563–571.
Willis, B. (1893) Mechanics of Appalachian structure. *U.S. Geological Survey Annual Report* **13** (1891–1892), part 2, 217–281.
Wiltschko, D. V. and Chapple, W. M. (1977) Flow of weak rocks in the Appalachian Plateau folds. *Bulletin of the Americal Association of Petroleum Geologists* **61**, 653–670.
Wiltschko, D. V., Medwedeff, D. A. and Millson, H. E. (1985) Distribution and mechanisms of strain within rocks on the northwest ramp of Pine Mountain block, southern Appalachian foreland: A field test of theory. *Geological Society of America Bulletin* **96**, 426–435.
Wojtal, S. (1989) Measuring displacement gradients and strains in faulted rock. *Journal of Structural Geology* **11**, 669–677.
Woodward, N. B. (1992) Deformation styles and geometric evolution of some Idaho–Wyoming thrust belt structures. In *Structural Geology of Fold and Thrust Belts*, eds S. Mitra and G. Fisher, pp. 191–206. The Johns Hopkins Studies in Earth and Space Sciences, **5**.
Wu, S. and Groshong, R. H. (1991) Low-temperature deformation of sandstone, southern Appalachian fold–thrust belt. *Geological Society of America Bulletin* **103**, 861–875.
Yeats, R. S., Huftile, G. J. and Grigsby, F. B. (1988) Oak Ridge fault, Ventura fold belt, and the Sisar décollement, Ventura basin, California. *Geology* **16**, 1112–1116.
Zoetemeijer, R., Sassi, W., Roure, F. and Cloetingh, S. (1992) Stratigraphic and kinematic modeling of thrust evolution, northern Apennines, Italy. *Geology* **20**, 1035–1038.

APPENDIX

Table A1. Microstructural abundances

Deformation mechanism	Microstructure	Structural domain* Forelimb (14)	Hinge (7)	Backlimb-flat (5)	Backlimb-ramp (11)	Footwall (5)	All domains (42)
Dislocation glide	Undulatory extinction	46	43	39	42	42	42
	Deformation lamellae	5	6	8	9	7	7
	Deformation bands	7	9	8	9	8	8
Micro-fracturing	Fluid inclusion planes (FIPs)	5	8	7	4	2	6
	Microveins	1	2	1	1	0.5	1
	Cataclastic bands	1	2	0	0	0	0.6
Pressure solution	Stylolites	0.5	0	0	0	0	0.1
	Sutured grains	0.5	0.2	0	0.1	0.2	0.2
None	None	58	52	60	56	64	56

*Parenthetical numbers are number of stations in that domain. Other numbers are percentage of grains with a particular structure. Totals of percentages for a column exceed 100% because some grains contained more than one microstructure. 250 counts for each sample.

Table A2. Strain ellipses measured with the PSS method

Sample	*b*-section					*p*-section					*v*-section					Total % volume loss
	Long axis	Short axis	Axial ratio	Axial rake	% Area loss	Long axis	Short axis	Axial ratio	Axial rake	% Area loss	Long axis	Short axis	Axial ratio	Axial rake	% Area loss	
N1	0.84	0.78	1.08	136	34	0.82	0.79	1.04	137	35	0.86	0.85	1.01	0	27	
N2	0.84	0.83	1.01	139	30	0.80	0.77	1.04	19	38	0.85	0.83	1.02	90	29	
N3	0.84	0.82	1.02	90	31	0.80	0.76	1.05	90	39	0.85	0.81	1.05	0	31	−35
N7	0.81	0.81	1.00	0	34	0.84	0.82	1.02	90	31	0.86	0.85	1.01	90	27	−30
N9	0.87	0.87	1.00	0	24	0.88	0.86	1.02	0	24	0.90	0.87	1.03	33	22	
N12	0.87	0.85	1.02	0	26	0.87	0.85	1.02	0	26	0.85	0.83	1.02	90	29	−29
N13	0.87	0.85	1.02	0	26	0.85	0.85	1.00	0	28	0.85	0.85	1.00	0	28	39
N14	0.89	0.86	1.03	0	23	0.89	0.86	1.03	0	23	0.88	0.87	1.01	0	23	−24
N16	0.86	0.85	1.01	0	27	0.87	0.85	1.02	0	26	0.87	0.85	1.02	0	26	−27
FN1	0.86	0.78	1.10	0	33	0.87	0.85	1.02	0	26	0.85	0.83	1.02	90	29	−32
S2	0.87	0.83	1.05	90	28	0.85	0.85	1.00	0	28	0.91	0.85	1.07	0	23	−26
S5	0.89	0.88	1.01	90	22	0.86	0.84	1.02	0	28	0.88	0.88	1.00	0	23	−24
S7	0.89	0.87	1.02	90	23	0.90	0.88	1.02	90	21	0.92	0.87	1.06	153	20	
S9	0.91	0.85	1.07	128	23	0.90	0.86	1.05	0	23	0.90	0.86	1.05	0	23	
S12	0.87	0.86	1.01	0	25	0.87	0.86	1.01	0	25	0.87	0.85	1.02	0	26	−26
S14	0.88	0.86	1.02	0	24	0.88	0.86	1.02	90	24	0.88	0.84	1.05	0	26	−27
S16	0.87	0.86	1.01	0	25	0.88	0.85	1.04	41	25	0.88	0.85	1.04	90	25	
S19	0.87	0.87	1.00	0	24	0.88	0.87	1.01	132	23	0.87	0.85	1.02	0	26	
S22	0.88	0.87	1.01	0	23	0.90	0.87	1.03	0	22	0.87	0.86	1.01	90	25	−25
FS1	0.89	0.81	1.10	137	28	0.86	0.82	1.05	0	29	0.86	0.84	1.02	0	28	−31

Rake measured in the plane of bedding with strike as a common reference frame.